


## Article

# Tailoring Metal–Oxide Interfaces via Selectively CeO<sub>2</sub>-Decorated Pd Nanocatalysts with Enhanced Catalytic Performance

Ziwen Liu <sup>1,2</sup>, Guizhen Zhang <sup>1,\*</sup>, Lijuan Niu <sup>3</sup>, Zaicheng Sun <sup>4</sup> , Zhenguo Li <sup>5,\*</sup> and Hong He <sup>1</sup>

<sup>1</sup> Beijing Key Laboratory for Green Catalysis and Separation, College of Materials Science & Engineering, Beijing University of Technology, Beijing 100124, China; liuzw2023.chji@sinopec.com (Z.L.)

<sup>2</sup> Institute of Engineering Technology, Sinopec Catalyst Co., Ltd., Beijing 101111, China

<sup>3</sup> Carbon Energy Technology Co., Ltd., Beijing 102400, China; nlj@carbonenergy.com.cn

<sup>4</sup> Center of Excellence for Environmental Safety and Biological Effects, Beijing Key Laboratory for Green Catalysis and Separation, Department of Chemistry, College of Chemistry and Life Science, Beijing University of Technology, Beijing 100124, China; sunzc@bjut.edu.cn

<sup>5</sup> China Automotive Technology and Research Center Co., Ltd., Tianjin 300300, China

\* Correspondence: zhangguizhen@bjut.edu.cn (G.Z.); lizhenguo@catarc.ac.cn (Z.L.)

**Abstract:** Metal–oxide interfaces play a prominent role in heterogeneous catalysis. Tailoring the metal–oxide interfaces effectively enhance the catalytic activities and thermal stability of noble metal catalysts. In this work, polyvinyl alcohol-protected reduction and L-arginine induction methods are adopted to prepare Pd catalysts (Pd/Al<sub>2</sub>O<sub>3</sub>-xCeO<sub>2</sub>) that are selectively decorated by CeO<sub>2</sub>, which form core–shell-like structures and generate more Pd–CeO<sub>2</sub> interfacial sites, so that the three-way catalytic activity of Pd/Al<sub>2</sub>O<sub>3</sub>-xCeO<sub>2</sub> catalysts is obviously significantly enhanced due to more adsorption oxygen at the interface of Pd–CeO<sub>2</sub> and good low-temperature reducibility. At the moment, the Pd/Al<sub>2</sub>O<sub>3</sub>-xCeO<sub>2</sub> catalysts exhibit excellent thermal stability after being calcined at 900 °C for 5 h, owing to the Pd species being highly redispersed on CeO<sub>2</sub> and part of the Pd species being incorporated into the lattice of CeO<sub>2</sub>. This is a major reason for the Pd/Al<sub>2</sub>O<sub>3</sub>-xCeO<sub>2</sub> catalysts to maintain high catalytic activity after aging at high temperatures. It is concluded that the metal–oxide interfaces and the interaction between Pd NPs and CeO<sub>2</sub> are responsible for the excellent catalytic performance and stability of Pd/Al<sub>2</sub>O<sub>3</sub>-xCeO<sub>2</sub> catalysts in three-way reactions.

**Keywords:** metal–oxide interface; selectively coating; thermal stability; three-way catalytic activity



Academic Editor: Uwe Burghaus

Received: 31 December 2024

Revised: 24 January 2025

Accepted: 24 January 2025

Published: 27 January 2025

**Citation:** Liu, Z.; Zhang, G.; Niu, L.; Sun, Z.; Li, Z.; He, H. Tailoring Metal–Oxide Interfaces via Selectively CeO<sub>2</sub>-Decorated Pd Nanocatalysts with Enhanced Catalytic Performance. *Nanomaterials* **2025**, *15*, 197. <https://doi.org/10.3390/nano15030197>

**Copyright:** © 2025 by the authors. Licensee MDPI, Basel, Switzerland. This article is an open access article distributed under the terms and conditions of the Creative Commons Attribution (CC BY) license (<https://creativecommons.org/licenses/by/4.0/>).

## 1. Introduction

Heterogeneous catalyst systems consisting of metals and oxide supports are widely used. Particularly, nano-sized metal particles have been extensively researched in the field of catalysis in recent years due to their high surface to volume ratios and effective catalytic performance [1,2]. Particularly when dispersed on oxide supports, their catalytic activities are greatly enhanced compared to those of pure metal particles or oxide supports because of the interaction between noble metal particles and oxide [3]. It is generally believed that the catalytic active site is located at the metal–oxide interface, which suggests that the rational design of the metal–oxide interface is critical for a highly efficient catalytic system [4]. However, it is limited to the contact area of the metal–oxide interface in traditional supported catalysts.

In addition, owing to their high surface area and surface energy, noble metal nanoparticles (NPs) on supported catalysts tend to aggregate into larger particles to minimize their surface energy, especially during catalytic reaction at high temperatures, which could easily

lead to their deactivation or the loss of catalytic activity [5,6]. For example, palladium (Pd) is the main active ingredient in most three-way catalysts (TWCs), usually loaded on an  $\text{Al}_2\text{O}_3$  support, which can convert CO, HC, and  $\text{NO}_x$  pollutants into non-toxic substances for controlling automobile exhaust emissions [7,8]. In addition, as one of the most commonly used reducible oxides,  $\text{CeO}_2$  is widely used because of its high oxygen storage capacity and excellent redox properties, and it also plays an important role in promoting the dispersion of noble metals in TWCs [9]. However, in order to meet increasingly stringent emission standards over the life of vehicles, the TWC is often installed in a close-coupled position near the exhaust manifold outlet to allow for quickly achieving light-off temperature after a cold start. During the warming-up of the engine, the temperature in this position can sometimes even reach up to  $1000\text{ }^\circ\text{C}$  [8]. Such a high temperature severely leads to catalysts' deactivation or the sintering of noble metal [10,11].

In summary, in order to prepare catalysts with high activity and excellent thermal stability, various strategies have been reported. In particular, core-shell nanostructures with inorganic oxide coatings are the ideal solution approaches, and have been widely researched recently [12–20]. Joo et al. reported the design of a high-temperature-stable model catalytic system that consisted of a Pt metal core coated with a mesoporous silica shell ( $\text{Pt@mSiO}_2$ ), which showed high thermal stability against metal particle agglomeration or sintering even after being subjected to  $750\text{ }^\circ\text{C}$  in air. The  $\text{Pt@mSiO}_2$  catalysts still keep the structure of Pt cores encaged within silica shells [12]. However, the etching process requires tedious steps and is time-consuming. Li and coworkers designed the hydrothermal stability of TWCs of core-shell  $\text{Pd@Ce}_{0.5}\text{Zr}_{0.5}\text{O}_2/\text{Al}_2\text{O}_3$  catalysts, and the Pd NPs remained isolated when the catalysts were calcined at  $1050\text{ }^\circ\text{C}$  in the presence of 10% water, but the catalytic activity of a fresh  $\text{Pd@Ce}_{0.5}\text{Zr}_{0.5}\text{O}_2/\text{Al}_2\text{O}_3$  catalyst is much lower than  $\text{Pd}/\text{Al}_2\text{O}_3$  [10]. This reduction in activity can be attributed to the blocking of active sites by the protective layer, which is a major deterrent to the practical utilization of these catalysts. Lu et al. designed a coking- and sintering-resistant palladium catalyst by atomic layer deposition (ALD), which can enhance the catalytic activity and stability of the  $\text{Pd}/\text{Al}_2\text{O}_3$  catalyst for the oxidative dehydrogenation of ethane. ALD, an advanced technology, can precisely control the thickness and position of the overcoating by a self-limiting growth process [21]. However, the method needs special instruments, and the precursors used are expensive, so they cannot be prepared on a large scale.

To overcome these challenges mentioned above, we report a facile way to precisely synthesize  $\text{Pd}/\text{Al}_2\text{O}_3\text{-xCeO}_2$  catalysts with excellent catalytic activity and thermal stability, in which  $\text{CeO}_2$  selectively decorated the Pd NPs supported on  $\text{Al}_2\text{O}_3$  by the L-arginine induction method to enlarge the metal-oxide interface. The physicochemical properties of the synthesized catalysts were characterized by a series of test methods, including TEM, XRD, BET,  $\text{H}_2$ -TPR, XPS,  $\text{O}_2$ -TPD, CO pulse adsorption, and so on. The results show that the oxygen adsorption capacity, low-temperature reducibility, and thermal stability of the catalysts can be significantly improved by constructing a rich Pd- $\text{CeO}_2$  interface. We believe that this work could provide a more fundamental understanding and means to improve catalytic performance by modulating the metal-oxide interface.

## 2. Experiment

### 2.1. Materials

Poly(vinyl pyrrolidone) (PVP, MW = 58,000), polyvinyl alcohol (PVA, 98–99% hydrolyzed, low molecular weight), aluminum oxide ( $\text{Al}_2\text{O}_3$ , NanoTek, 99.5%), and L-arginine (98.0%) were obtained from Alfa Aesar (Shanghai, China) Chemicals Co., Ltd. Ascorbic acid (AR 99.0%) and KBr (SP 99.0%) were purchased from Sinopharm (Beijing, China) Chemical Reagent Co., Ltd.  $\text{Na}_2\text{PdCl}_4$  (99.9%) was purchased from J&K Chemical (Beijing, China).

$\text{Ce}(\text{NO}_3)_3 \cdot 6\text{H}_2\text{O}$  (AR 99.0%) and  $\text{NaBH}_4$  (AR 98.0%) were obtained from Tianjin Fuchen Chemical Reagents Factory (Tianjin, China).

## 2.2. Catalyst Preparation

We undertook the synthesis of  $\text{Pd}/\text{Al}_2\text{O}_3\text{-xCeO}_2$  fresh catalysts through polyvinyl alcohol-protected reduction and L-arginine induction methods. First,  $\text{Pd}/\text{Al}_2\text{O}_3$  catalysts were synthesized by a PVA-protected reduction strategy [22]. The typical steps are as follows: The required amount of PVA (noble metal/PVA mass ratio = 1:1.5) was added to an aqueous solution of  $\text{Na}_2\text{PdCl}_4$  and stirred vigorously in an ice bath for 20 min. A rapid injection of  $\text{NaBH}_4$  (2 g/L, molar ratio of noble metal/ $\text{NaBH}_4$  = 1:5) produced a dark-colored sol. A certain weight of  $\text{Al}_2\text{O}_3$  power was then added to the dark-colored sol under stirring until complete adsorption. The resulting mixture was filtered, washed with deionized water, and dried at 80 °C overnight. The loading of Pd species was adjusted by controlling the additional amount of  $\text{Al}_2\text{O}_3$  power. The  $\text{Pd}/\text{CeO}_2$  catalyst was prepared by similar methods just by replacing  $\text{Al}_2\text{O}_3$  with  $\text{CeO}_2$ .

Then, the L-arginine induction method was used to synthesize  $\text{Pd}/\text{Al}_2\text{O}_3\text{-xCeO}_2$  catalysts by  $\text{CeO}_2$ , which selectively decorated the Pd nanoparticles supported on the  $\text{Al}_2\text{O}_3$ . The detailed process is as shown below: A desired amount of dried  $\text{Pd}/\text{Al}_2\text{O}_3$  catalysts was dispersed in 30 mL deionized water under vigorous stirring for 1 h and followed by dropping in 10 mL L-arginine solution (L-arginine/ $\text{Ce}(\text{NO}_3)_3 \cdot 6\text{H}_2\text{O}$  molar ratio = 3.5:1 in 10 mL  $\text{H}_2\text{O}$ ) at room temperature under vigorous stirring for 40 min. Next, a certain molar amount of  $\text{Ce}(\text{NO}_3)_3 \cdot 6\text{H}_2\text{O}$  was dissolved in a mixture solution of 20 mL  $\text{H}_2\text{O}$  and 20 mL ethanol, then was added into the above system under vigorous stirring for 10 min. Finally, the mixture was heated at 80 °C for 12 h. The obtained mixture was filtered, washed with deionized water, and dried at 120 °C overnight. Finally, the  $\text{Pd}/\text{Al}_2\text{O}_3\text{-xCeO}_2$  fresh catalyst was obtained by calcining the sample from RT to 500 °C in the air at a ramp rate of 5 °C/min and maintaining this temperature for 3 h. The content of  $\text{CeO}_2$  was regulated by changing the additional amount of  $\text{CeO}_2$ .

In addition, the  $\text{Pd}/\text{Al}_2\text{O}_3\text{-xCeO}_2\text{-JZ}$  catalyst was synthesized by a conventional wet impregnation method. First, a certain amount of dried  $\text{Pd}/\text{Al}_2\text{O}_3$  catalysts was dispersed in certain molar amounts of  $\text{Ce}(\text{NO}_3)_3 \cdot 6\text{H}_2\text{O}$  solution under vigorous stirring, and then the slurry was vaporized with sonication (60 kHz) at 80 °C, followed by drying at 120 °C for 12 h.

The methodology developed by Xia's team was employed to fabricate Pd nanoparticles (NPs) supported on  $\text{Al}_2\text{O}_3$ , with diameters of 12 nm and 19 nm, for use as  $\text{Pd}/\text{Al}_2\text{O}_3$  catalysts (designated as x nm  $\text{Pd}/\text{Al}_2\text{O}_3$ ) [1]. The synthesis procedure is outlined as follows: An aqueous solution containing 50 mg of polyvinylpyrrolidone (PVP), 60 mg of ascorbic acid, and either 300 mg or 450 mg of potassium bromide (KBr) was introduced into a flask, amounting to a total volume of 8.0 mL. This solution was preheated to 80 °C in an oil bath while being subjected to magnetic stirring for a duration of 10 min. Following this, 3.1 mL of a sodium tetrachloropalladate ( $\text{Na}_2\text{PdCl}_4$ ) aqueous solution with a concentration of 0.0625 M was introduced into the mixture. The reaction was allowed to proceed for 3 h at a constant temperature of 80 °C. Afterward, the resulting product was isolated via centrifugation and subsequently rinsed with acetone and ethanol to eliminate any surplus PVP. The purified Pd NPs were then redispersed in 20 mL of ethanol under vigorous stirring, into which a measured quantity of  $\text{Al}_2\text{O}_3$  support was added until complete adsorption was achieved. The resulting mixture was centrifuged, washed with deionized water, and dried at 120 °C for 12 h to prepare the x nm  $\text{Pd}/\text{Al}_2\text{O}_3$  catalysts for further use. The x nm  $\text{Pd}/\text{Al}_2\text{O}_3\text{-xCeO}_2$  and x nm  $\text{Pd}/\text{Al}_2\text{O}_3\text{-xCeO}_2\text{-JZ}$  catalysts were synthesized

using L-arginine-induced methods and the conventional wet impregnation technique previously described.

All of the fresh catalysts were calcined at 500 °C for 3 h in a furnace. For the aged catalysts, the catalysts were calcined at 900 °C in air for 5 h to obtain aged catalysts. The actual loading of the catalysts was determined by ICP-AES as shown in Table S1.

### 2.3. Evaluation of Catalytic Performance

The three-way catalytic performances over the catalysts were evaluated in a fixed-bed reactor (i.d. = 8 mm). The catalyst (200 mg) was fixed in the middle of the reactor by packing quartz wool at both ends. The reaction temperature was monitored by a thermocouple located at the bed of the catalyst. The reaction mixture contained 1.6% CO, 0.05% HC (propane/propene = 2/1), 0.1% NO<sub>x</sub>, 1.0% O<sub>2</sub>, 0.23% H<sub>2</sub>, and N<sub>2</sub> as balance gas. The corresponding space velocity (SV) was 300,000 mL·(g·h)<sup>-1</sup>. The concentrations of CO, NO<sub>x</sub>, and HC in the inlet and outlet of the reactor were analyzed on a Horiba MEXA-584L automobile emission analyzer. In this work, *T*<sub>90</sub> (corresponding to the temperature at which the 90% conversion of a given compound is completed) was used to evaluate the activities of different catalysts.

### 2.4. Characterizations

The catalysts were characterized using a series of test methods such as TEM, XRD, BET, H<sub>2</sub>-TPR, XPS, O<sub>2</sub>-TPD, and so on. The detailed catalyst characterizations and catalytic evaluation procedures are described in the Supplementary Materials.

## 3. Results and Discussion

### 3.1. Characterization of Fresh Catalysts

#### 3.1.1. Morphology Analysis

The high-resolution transmission electron microscopy (HRTEM) images of the irregularly shaped Pd nanoparticles are depicted in Figure S1. These nanoparticles exhibited an average diameter of approximately 4 nm, with a lattice spacing of 0.22 nm, which is consistent with the (111) planes of Pd nanocrystals [1]. Following the deposition of these Pd nanoparticles onto Al<sub>2</sub>O<sub>3</sub>, the transmission electron microscopy (TEM) and HRTEM images of the pristine Pd/Al<sub>2</sub>O<sub>3</sub> catalyst are presented in Figure 1A,E, respectively. The Pd nanoparticles were uniformly dispersed on the Al<sub>2</sub>O<sub>3</sub> support, with a lattice spacing of 0.263 nm. This observation is indicative of the (101) crystallographic plane of PdO, suggesting that the metallic Pd nanoparticles were oxidized to PdO upon heating to 500 °C.

TEM images of the fresh Pd/Al<sub>2</sub>O<sub>3</sub>-xCeO<sub>2</sub> catalysts are presented in Figure 1B–D,F–H, revealing numerous tiny CeO<sub>2</sub> NPs supported on the surface of Pd/Al<sub>2</sub>O<sub>3</sub>, resembling an incomplete shell. Given that the size of the Pd nanoparticles is approximately 4 nm, which is similar to the size range of the CeO<sub>2</sub> nanoparticles (3–7 nm) as determined by the Scherrer equation (Table 1), it becomes challenging to distinguish between Pd and CeO<sub>2</sub> nanoparticles using TEM and HRTEM. Furthermore, the HRTEM images indicate lattice spacings of 0.27 nm and 0.31 nm, which correspond to the (200) and (111) planes of the fluorite-phase CeO<sub>2</sub>, respectively. To further analyze the distribution of Pd and CeO<sub>2</sub> components within these catalysts, energy-dispersive X-ray spectroscopy (EDS) mapping analyses were conducted. The results for the fresh Pd/Al<sub>2</sub>O<sub>3</sub>-1.2CeO<sub>2</sub> catalyst are depicted in Figure S2. It is observed that the Pd nanoparticles supported on the Al<sub>2</sub>O<sub>3</sub> are encircled by CeO<sub>2</sub> nanoparticles; however, the evidence is insufficient to conclusively demonstrate that the Pd nanoparticles on Al<sub>2</sub>O<sub>3</sub> can be selectively decorated by CeO<sub>2</sub> nanoparticles.

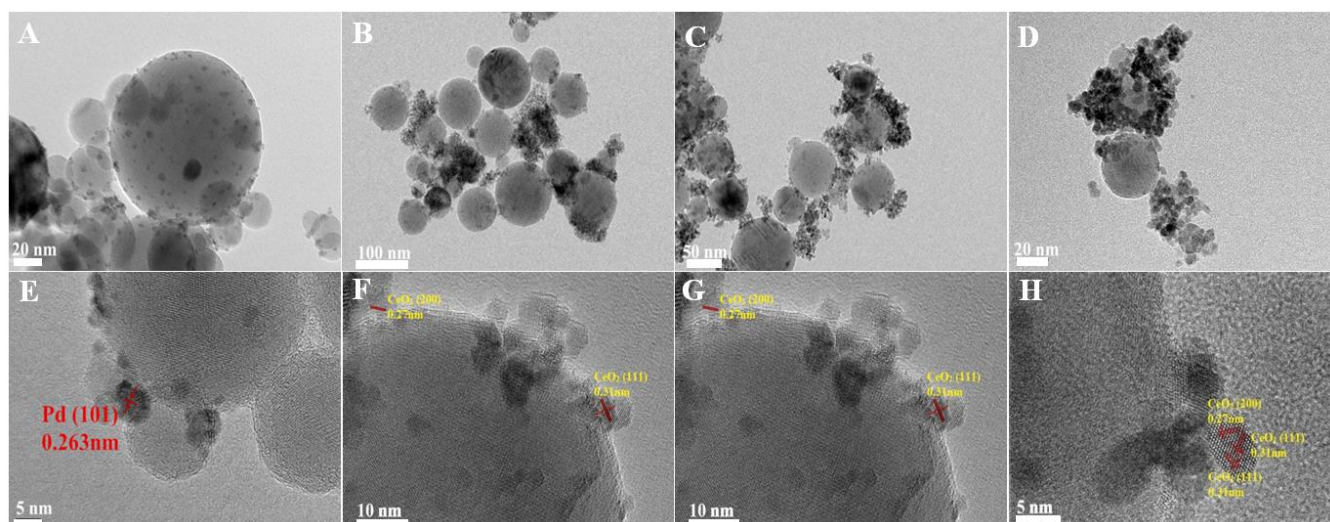


**Figure 1.** TEM and HRTEM of fresh (A,E) Pd/Al<sub>2</sub>O<sub>3</sub>, (B,F) Pd/Al<sub>2</sub>O<sub>3</sub>-1.2CeO<sub>2</sub>, (C,G) Pd/Al<sub>2</sub>O<sub>3</sub>-2.4CeO<sub>2</sub>, (D,H) Pd/Al<sub>2</sub>O<sub>3</sub>-3.0CeO<sub>2</sub> catalysts.

**Table 1.** BET surface areas, pore volumes, average sizes ( $D_{\text{CeO}_2}$ ), and dispersion of the as-obtained catalysts.

Fresh Catalysts	Surface Area (m <sup>2</sup> ·g <sup>-1</sup> )	Pore Volume (cm <sup>3</sup> ·g <sup>-1</sup> )	$D_{\text{CeO}_2}$ <sup>a</sup> (nm)	Dispersion of Pd <sup>b</sup> (%)
Pd/Al <sub>2</sub> O <sub>3</sub>	34	0.193	—	27.8
Pd/Al <sub>2</sub> O <sub>3</sub> -1.2CeO <sub>2</sub>	56	0.248	5.5	18.7
Pd/Al <sub>2</sub> O <sub>3</sub> -2.4CeO <sub>2</sub>	62	0.231	6.7	16.4
Pd/Al <sub>2</sub> O <sub>3</sub> -3.0CeO <sub>2</sub>	71	0.220	7.1	15.2
Pd/Al <sub>2</sub> O <sub>3</sub> -2.4CeO <sub>2</sub> -JZ	46	0.140	7.5	22.1

<sup>a</sup> Data were obtained according to the Scherrer equation using the FWHM of CeO<sub>2</sub> in the XRD patterns. <sup>b</sup> Data were obtained by the CO pulse method.

To conclusively demonstrate the selective decoration of Pd nanoparticles (NPs) by CeO<sub>2</sub> nanoparticles (NPs), larger Pd NPs with diameters of 12 nm and 19 nm were synthesized, as shown in Figure S3. The energy-dispersive X-ray spectroscopy (EDS) mapping images of the fresh 12 nm Pd/Al<sub>2</sub>O<sub>3</sub>-1.2CeO<sub>2</sub> catalysts are displayed in Figures S4–S6. These images clearly reveal the formation of a typical core–shell structure, with Pd NPs surrounded by a multitude of CeO<sub>2</sub> NPs, signifying the creation of a core–shell configuration and an abundance of Pd–CeO<sub>2</sub> interfaces. A similar phenomenon was observed in the 19 nm Pd/Al<sub>2</sub>O<sub>3</sub>-1.2CeO<sub>2</sub> catalysts, where Pd NPs were centrally located and enveloped by a shell of dispersed CeO<sub>2</sub> NPs, confirming core–shell structure formation. However, the elemental distribution in the fresh catalysts of 12 nm Pd/Al<sub>2</sub>O<sub>3</sub>-2.4CeO<sub>2</sub>-JZ and 19 nm Pd/Al<sub>2</sub>O<sub>3</sub>-1.2CeO<sub>2</sub>-JZ was also examined, as depicted in Figures S7–S9. It was evident that CeO<sub>2</sub> was scattered across the surface of the Al<sub>2</sub>O<sub>3</sub>, following the distribution of Al<sub>2</sub>O<sub>3</sub>, which suggests that CeO<sub>2</sub> could not selectively decorate Pd NPs when using the traditional wet impregnation method. Based on the aforementioned results, it can be concluded that Pd NPs supported on Al<sub>2</sub>O<sub>3</sub> can be selectively decorated by CeO<sub>2</sub> NPs through the L-arginine induction method, leading to the formation of numerous Pd–CeO<sub>2</sub> interfaces.

### 3.1.2. Pore Structure Properties

Analysis of the nitrogen adsorption–desorption isotherms revealed that all catalysts exhibited a Type IV isotherm, as shown in Figure S10. The presence of an H3 hysteresis loop without a saturation plateau at relatively high pressures (0.7–1.0) indicates the presence of irregular mesopores. The specific surface areas and total pore volumes for the Pd/Al<sub>2</sub>O<sub>3</sub>,

Pd/Al<sub>2</sub>O<sub>3</sub>-xCeO<sub>2</sub>, and Pd/Al<sub>2</sub>O<sub>3</sub>-2.4CeO<sub>2</sub>-JZ catalysts are detailed in Table 1. For the fresh Pd/Al<sub>2</sub>O<sub>3</sub>-xCeO<sub>2</sub> catalysts, the surface area increased while the total pore volume decreased with the gradual increase in CeO<sub>2</sub> content. When compared to the Pd/Al<sub>2</sub>O<sub>3</sub> and Pd/Al<sub>2</sub>O<sub>3</sub>-2.4CeO<sub>2</sub>-JZ catalysts, the Pd/Al<sub>2</sub>O<sub>3</sub>-xCeO<sub>2</sub> catalysts displayed a larger surface area and total pore volume, ranging from 56 to 71 m<sup>2</sup>/g and from 0.248 to 0.220 cm<sup>3</sup>/g, respectively. It is generally accepted that the increased pore volume and specific surface area contribute significantly to the enhanced catalytic performance observed in the fresh Pd/Al<sub>2</sub>O<sub>3</sub>-xCeO<sub>2</sub> catalysts. However, when considering the subsequent catalytic activity, the Pd/Al<sub>2</sub>O<sub>3</sub>-1.2CeO<sub>2</sub> catalyst demonstrated the best performance, despite having a smaller surface area compared to the Pd/Al<sub>2</sub>O<sub>3</sub>-2.4CeO<sub>2</sub> and Pd/Al<sub>2</sub>O<sub>3</sub>-3.0CeO<sub>2</sub> catalysts. This suggests that surface area is not the primary factor influencing catalytic activity.

### 3.1.3. Crystal Phase Analysis

Figure 2A presents the X-ray diffraction (XRD) patterns for both fresh and aged Pd/Al<sub>2</sub>O<sub>3</sub>, Pd/Al<sub>2</sub>O<sub>3</sub>-xCeO<sub>2</sub>, and Pd/Al<sub>2</sub>O<sub>3</sub>-2.4CeO<sub>2</sub>-JZ catalysts, with the crystallite sizes of the CeO<sub>2</sub> phases tabulated in Table 1. In the fresh catalysts, the diffraction patterns attributable to Al<sub>2</sub>O<sub>3</sub> and CeO<sub>2</sub> correspond to the  $\delta$ -Al<sub>2</sub>O<sub>3</sub> phase (JCPDS No. 46-1215) and the cubic phase (JCPDS No. 34-0394), respectively. Notably, no distinct Pd phase peaks are observed in these fresh catalysts, which can be attributed to the relatively low Pd loading or the fine dispersion of Pd species on the Al<sub>2</sub>O<sub>3</sub> surface.

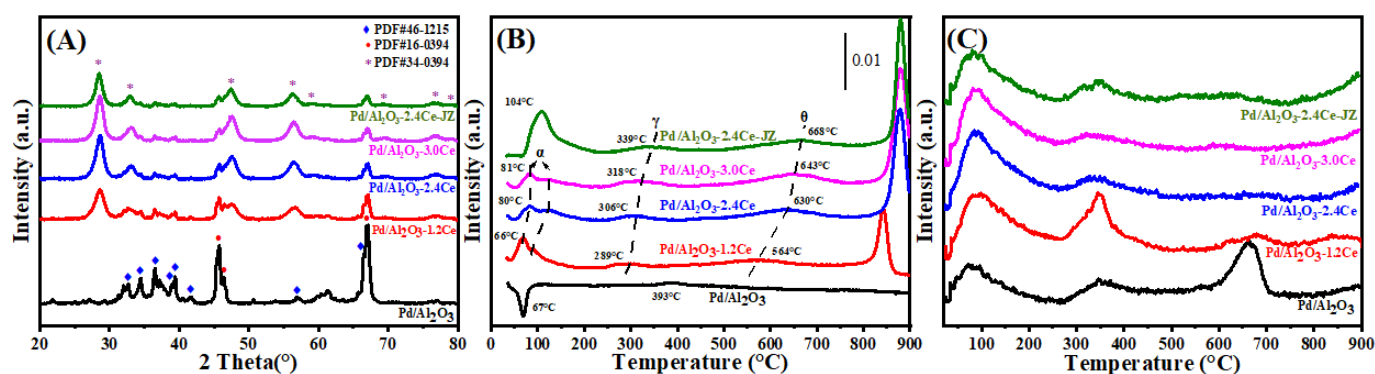


Figure 2. (A) XRD patterns, (B) H<sub>2</sub>-TPR profiles, and (C) O<sub>2</sub>-TPD profiles of the fresh catalysts.

### 3.1.4. Low-Temperature Reducibility Analysis

H<sub>2</sub>-TPR profiles of the Pd/Al<sub>2</sub>O<sub>3</sub>, Pd/Al<sub>2</sub>O<sub>3</sub>-xCeO<sub>2</sub>, and Pd/Al<sub>2</sub>O<sub>3</sub>-2.4CeO<sub>2</sub>-JZ fresh catalysts are displayed in Figure 2B. Furthermore, the values of H<sub>2</sub> consumption are calculated using the CuO sample as a standard with a similar TPR procedure, and the results are summarized in Table 2.

Table 2. H<sub>2</sub> consumption and surface element composition of the fresh catalysts.

Fresh Catalysts	Reducibility of Fresh Catalysts (H <sub>2</sub> Consumption (μmol/gcat))					Fresh-Surface Element Composition Molar Ratio (%)	
	Negative Peak	<200 °C	200–250 °C	250–350 °C	500–750 °C	O <sub>ads</sub> /O <sub>latt</sub>	Ce <sup>3+</sup> /(Ce <sup>3+</sup> + Ce <sup>4+</sup> )
Pd/Al <sub>2</sub> O <sub>3</sub>	−26.0	—	6.5	—	—	—	—
Pd/Al <sub>2</sub> O <sub>3</sub> -1.2CeO <sub>2</sub>	—	88.7	—	18.2	43.2	8.1	16.4
Pd/Al <sub>2</sub> O <sub>3</sub> -2.4CeO <sub>2</sub>	—	76.8	—	21.8	102.1	7.9	17.7
Pd/Al <sub>2</sub> O <sub>3</sub> -3.0CeO <sub>2</sub>	—	69.9	—	41.5	112.2	6.0	18.1
Pd/Al <sub>2</sub> O <sub>3</sub> -2.4CeO <sub>2</sub> -JZ	—	225.7	—	29.5	78.2	4.8	19.0

In the case of the Pd/Al<sub>2</sub>O<sub>3</sub> sample, a distinct negative peak is observed at 67 °C, corresponding to a hydrogen release of 26 μmol/g<sub>cat</sub>. This phenomenon can be ascribed to the decomposition of β-PdHx. Under conditions of low hydrogen pressure and ambient temperature within a hydrogen-rich environment, species like PdO are reduced to their metallic Pd form, which then adsorbs hydrogen to form β-PdHx species. Subsequently, a second peak emerges at a higher temperature of 393 °C, likely due to the reduction of a two-dimensional (2D) PdO surface phase. The formation of this 2D surface phase is hypothesized to occur during high-temperature oxidation processes [23]. This particular species is noted to be more resistant to reduction compared to the PdO species observed at lower temperatures [24].

For the fresh Pd/Al<sub>2</sub>O<sub>3</sub>-xCeO<sub>2</sub> catalysts, two reduction peaks below 200 °C are observed, which are attributed to the reduction of surface oxygen species associated with Pd sites or Pd interacting with ceria at the Pd-CeO<sub>2</sub> interface. This interface is considered the primary active site for Pd-supported catalysts [25]. In addition, the total H<sub>2</sub> consumption below 200 °C follows the order Pd/Al<sub>2</sub>O<sub>3</sub>-1.2CeO<sub>2</sub> (88.7 μmol/g<sub>cat</sub>) > Pd/Al<sub>2</sub>O<sub>3</sub>-2.4CeO<sub>2</sub> (76.8 μmol/g<sub>cat</sub>) > Pd/Al<sub>2</sub>O<sub>3</sub>-3.0CeO<sub>2</sub> (69.9 μmol/g<sub>cat</sub>). This indicates that Pd/Al<sub>2</sub>O<sub>3</sub>-1.2CeO<sub>2</sub> has the best low-temperature reducibility among the others, achieving the lowest reduction temperature. The low-temperature reducibility of a catalyst is typically correlated with its adsorbed oxygen species [26]. Furthermore, the Pd/Al<sub>2</sub>O<sub>3</sub>-2.4CeO<sub>2</sub>-JZ sample shows a higher reduction temperature than Pd/Al<sub>2</sub>O<sub>3</sub>-xCeO<sub>2</sub> catalysts at 104 °C, with a hydrogen consumption of 225.7 μmol/g<sub>cat</sub>, which is much larger than the theoretical value (94 μmol/g<sub>cat</sub>) required for reducing PdO to Pd<sup>0</sup>. This suggests the presence of a spillover phenomenon, where adsorbed hydrogen from the noble metal particles is transferred to the support due to the strong interaction between PdO and CeO<sub>2</sub>. This leads to the reduction of interfacial Ce<sup>4+</sup> at low temperatures. These findings indicate that there are distinct interactions between Pd nanoparticles and CeO<sub>2</sub> in the Pd/Al<sub>2</sub>O<sub>3</sub>-xCeO<sub>2</sub> and Pd/Al<sub>2</sub>O<sub>3</sub>-2.4CeO<sub>2</sub>-JZ catalysts prepared by different preparation methods.

The reduction peaks at higher temperatures (γ) were observed for the catalysts, which can be attributed to the hydrogen consumption of surface CeO<sub>2</sub> that is in close contact with the Pd species. Furthermore, a reduction peak (θ) at 550–700 °C is likely due to the reduction of surface Ce<sup>4+</sup> ions that are distant from Pd species [27]. Above 800 °C, the reduction peaks can be associated with the bulk reduction of CeO<sub>2</sub>. The H<sub>2</sub>-TPR results indicate that the Pd-CeO<sub>2</sub> interface, formed by the L-arginine induction method, exerts a more pronounced influence on the redox properties of the materials.

### 3.1.5. Oxygen Species Analysis

It is widely accepted that the capacity of catalysts to adsorb and activate oxygen species is a critical factor in heterogeneous catalysis. O<sub>2</sub>-TPD measurements were conducted on the fresh catalyst, as depicted in Figure 2C. The adsorbed oxygen typically undergoes the following sequence of transformations: O<sub>2</sub> (ad) → O<sub>2</sub><sup>-</sup> (ad) → O<sup>-</sup> (ad) → O<sup>2-</sup> (lattice) [28]. Generally, the desorption peak below 400 °C is attributed to the surface oxygen species (O<sub>ad</sub>), while those in the range of 600 to 700 °C correspond to the decomposition of palladium oxide into metallic palladium [29], which occurs at a significantly lower temperature than the bulk PdO (approximately 790 °C). This reduction in temperature is attributed to the fact that nanometer-sized materials typically have lower melting points than their bulk counterparts, owing to their increased surface area to volume ratio and elevated surface energy [30].

When comparing the O<sub>ad</sub> desorption peak areas between the Pd/Al<sub>2</sub>O<sub>3</sub>, Pd/Al<sub>2</sub>O<sub>3</sub>-2.4CeO<sub>2</sub>-JZ, and Pd/Al<sub>2</sub>O<sub>3</sub>-xCeO<sub>2</sub> catalysts by integrating peak area (summarizing in Table S2), the Pd/Al<sub>2</sub>O<sub>3</sub>-xCeO<sub>2</sub> catalysts were found to have a higher concentration of

surface oxygen species than the other catalysts in the following order: Pd/Al<sub>2</sub>O<sub>3</sub>-1.2CeO<sub>2</sub> > Pd/Al<sub>2</sub>O<sub>3</sub>-2.4CeO<sub>2</sub> > Pd/Al<sub>2</sub>O<sub>3</sub>-3.0CeO<sub>2</sub>. This sequence aligns with the observed catalytic activity, suggesting that the Pd-CeO<sub>2</sub> interface created by the L-arginine induction method enhances the absorption of oxygen species at 200 °C and 200–400 °C. As the amount of CeO<sub>2</sub> increases, the surface oxygen species obviously decrease, especially at 200–400 °C, likely because the Pd-CeO<sub>2</sub> interface becomes progressively obscured by excess CeO<sub>2</sub>, resulting in a slight decrease in catalytic activity. Furthermore, high-temperature desorption peaks between 600 °C and 700 °C were observed in these catalysts. However, the Pd/Al<sub>2</sub>O<sub>3</sub> sample shows a greater intensity than the other catalysts due to the decomposition of PdO<sub>x</sub> species. This indicates that catalysts containing CeO<sub>2</sub> have more stable PdO<sub>x</sub> species, which are beneficial for oxidation activity and catalytic thermal stability [31]. Considering both the abundance of surface oxygen species and the stability of PdO<sub>x</sub> species, it is anticipated that the Pd/Al<sub>2</sub>O<sub>3</sub>-xCeO<sub>2</sub> catalysts will exhibit superior catalytic performance compared to other catalysts.

### 3.1.6. Surface Composition and Metal Chemical Analysis

The surface element composition and surface species of fresh catalysts were evaluated by X-ray photoelectron spectroscopy (XPS). Figure 3 illustrates the Al 2p, O 1s, Pd 3d, and Ce 3d XPS spectra of the fresh catalysts, and the surface element compositions are summarized in Table 2. From Figure 3A, the chemical states of Al 2p spectra of all the catalysts can be described by a symmetric peak at a binding energy of 74.2–74.5 eV, which corresponds with the literature data for Al<sup>3+</sup> species in Al<sub>2</sub>O<sub>3</sub> [32,33].

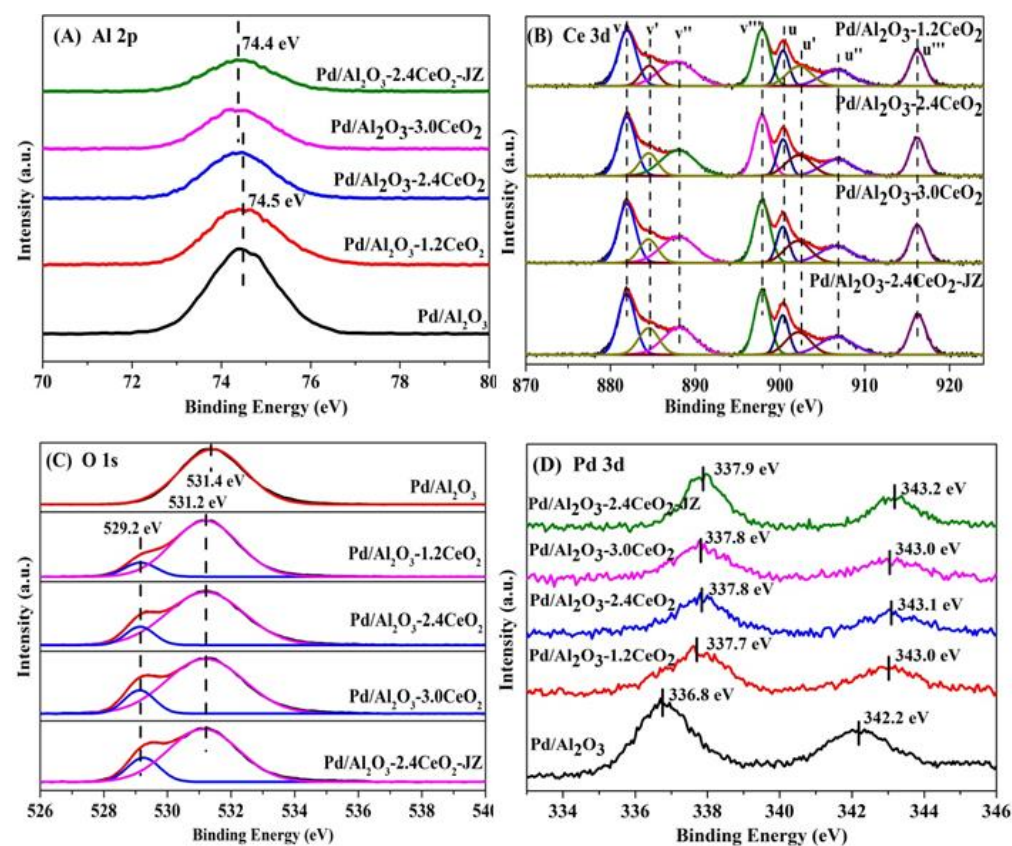


Figure 3. (A) Al 2p, (B) Ce 3d, (C) O 1s, and (D) Pd 3d XPS spectra of the fresh catalysts.

Figure 3B depicts the Ce 3d XPS spectra peaks labeled u and v corresponding to the 3d<sub>3/2</sub> and 3d<sub>5/2</sub> spin-orbit states of the Ce cations. The signals u' and v' belong to the Ce<sup>3+</sup> species, while others are ascribed to the Ce<sup>4+</sup> species [34,35], indicating that both



$\text{Ce}^{3+}$  and  $\text{Ce}^{4+}$  exist in the catalysts. It could be inferred that the oxygen vacancies are formed via the reduction of  $\text{Ce}^{4+}$  to  $\text{Ce}^{3+}$  in those catalysts, which is important to their redox properties and corresponding three-way activity [36,37]. Higher concentrations of  $\text{Ce}^{3+}$  species will produce more oxygen vacancies that exist in the catalysts. In addition, the surface  $\text{Ce}^{3+}$  concentration was analyzed by integrating the peak area of their respective valence states. As listed in Table 2, the value of  $\text{Ce}^{3+}$  concentration in the sequence of  $\text{Pd}/\text{Al}_2\text{O}_3\text{-}2.4\text{CeO}_2\text{-JZ}$  (19.0%) >  $\text{Pd}/\text{Al}_2\text{O}_3\text{-}3.0\text{CeO}_2$  (18.1%) >  $\text{Pd}/\text{Al}_2\text{O}_3\text{-}2.4\text{CeO}_2$  (17.7%) >  $\text{Pd}/\text{Al}_2\text{O}_3\text{-}1.2\text{CeO}_2$  (16.4%) differs from the results of catalytic activity, indicating the  $\text{Ce}^{3+}$  concentration seemingly was not the determining factor of catalytic activity.

It is widely accepted that catalysts with a higher concentration of adsorbed oxygen species are more effective for oxidation–reduction reactions [26,29]. Regarding the O 1s XPS spectra, the  $\text{Pd}/\text{Al}_2\text{O}_3$  catalysts showed only the presence of adsorbed oxygen. For the other catalysts, the asymmetrical O 1s spectrum could be deconvoluted into two components: the lattice oxygen ( $\text{O}_{\text{latt}}$ ) species at binding energies (BEs) of 529.1–529.2 eV and the surface adsorbed oxygen ( $\text{O}_{\text{ads}}$ ) species at BEs of 531.0–531.4 eV [38].  $\text{CeO}_2$  is renowned for its excellent oxygen storage and release capabilities due to the presence of cerium ions in mixed oxidation states, which can facilitate the redox process between  $\text{Ce}^{3+}$  and  $\text{Ce}^{4+}$ . Typically,  $\text{O}_2$  molecules can be adsorbed at the oxygen vacancies of  $\text{CeO}_2$  [39]. As shown in Table 2, the  $\text{O}_{\text{ads}}/\text{O}_{\text{latt}}$  molar ratio for the fresh catalysts decreased in the following order:  $\text{Pd}/\text{Al}_2\text{O}_3\text{-}1.2\text{CeO}_2$  (8.1) >  $\text{Pd}/\text{Al}_2\text{O}_3\text{-}2.4\text{CeO}_2$  (7.9) >  $\text{Pd}/\text{Al}_2\text{O}_3\text{-}3.0\text{CeO}_2$  (6.0) >  $\text{Pd}/\text{Al}_2\text{O}_3\text{-}2.4\text{CeO}_2\text{-JZ}$  (4.8). This order does not correspond to the variation in the  $\text{Ce}^{3+}/\text{Ce}^{4+}$  molar ratio among the catalysts, suggesting that adsorbed oxygen species are not only located at the surface oxygen vacancies of  $\text{CeO}_2$  and the surface of  $\text{Pd}/\text{Al}_2\text{O}_3$  but also that a significant amount of adsorbed oxygen exists at the interface between Pd nanoparticles and  $\text{CeO}_2$ . This indicates that the Pd- $\text{CeO}_2$  interface formed over the  $\text{Pd}/\text{Al}_2\text{O}_3\text{-}x\text{CeO}_2$  catalysts has a very strong oxygen adsorption capacity. Furthermore, the  $\text{O}_{\text{ads}}/\text{O}_{\text{latt}}$  molar ratio aligns with the order of catalytic activity variation, demonstrating that the concentration of adsorbed oxygen species is the primary factor influencing catalytic activity.

Furthermore, the Pd 3d spectra of the fresh catalysts have been subjected to analysis, as shown in Figure 3D. The fresh  $\text{Pd}/\text{Al}_2\text{O}_3$  catalyst exhibits a single Pd  $3d_{5/2}$  peak at 336.8 eV, which is characteristic of PdO [40]. The Pd  $3d_{5/2}$  spectra for  $\text{Pd}/\text{Al}_2\text{O}_3\text{-}1.2\text{CeO}_2$ ,  $\text{Pd}/\text{Al}_2\text{O}_3\text{-}2.4\text{CeO}_2$ ,  $\text{Pd}/\text{Al}_2\text{O}_3\text{-}3.0\text{CeO}_2$ , and  $\text{Pd}/\text{Al}_2\text{O}_3\text{-}2.4\text{CeO}_2\text{-JZ}$  are recorded at 337.7, 337.8, 337.8, and 337.9 eV, respectively. These values are shifted by 0.9, 1.0, 1.0, and 1.1 eV to higher binding energies relative to PdO, suggesting a strong Pd- $\text{CeO}_2$  interaction due to the electron transfer from the Pd to  $\text{CeO}_2$  support. This is attributed to the redox potential of  $\text{Pd}^{2+}/\text{Pd}^0$  being lower than that of  $\text{Ce}^{4+}/\text{Ce}^{3+}$  [41]. Compared to the binding energy of Pd  $3d_{5/2}$  spectra in  $\text{Pd}(\text{NO}_3)_2$  and  $\text{PdCl}_2$ , which are 337.7 eV and 337.8 eV, respectively [42], the Pd species in the aforementioned fresh catalysts are in a highly ionic state, indicating the strong interaction between Pd species and  $\text{CeO}_2$ . In addition, the intensity of the Pd  $3d_{5/2}$  peak for the  $\text{Pd}/\text{Al}_2\text{O}_3\text{-}x\text{CeO}_2$  fresh catalysts containing  $\text{CeO}_2$  is much lower than that of the  $\text{Pd}/\text{Al}_2\text{O}_3$  catalyst. This is because the Pd species are partially covered by  $\text{CeO}_2$  but not entirely obscured, which is consistent with the result of the metal dispersion of Pd species as presented in Table 1.

### 3.1.7. Three-Way Catalytic Activities of Fresh Catalysts

Figure 4 and Table S3 present the conversion results of CO, HC, and NO under stoichiometric conditions over the fresh catalysts. The  $T_{90}$  values, which represent the temperatures at which the 90% conversion of a given compound is achieved, are used to assess the activities of the different catalysts. Among the fresh catalysts,  $\text{Pd}/\text{Al}_2\text{O}_3\text{-}x\text{CeO}_2$  catalysts demonstrate excellent catalytic activities in the removal of three contaminations

compared to the Pd/Al<sub>2</sub>O<sub>3</sub> catalysts, with the order being Pd/Al<sub>2</sub>O<sub>3</sub>-1.2CeO<sub>2</sub> ≥ Pd/Al<sub>2</sub>O<sub>3</sub>-2.4CeO<sub>2</sub> ≥ Pd/Al<sub>2</sub>O<sub>3</sub>-3.0CeO<sub>2</sub> > Pd/Al<sub>2</sub>O<sub>3</sub>. Notably, the Pd/Al<sub>2</sub>O<sub>3</sub>-1.2CeO<sub>2</sub> catalyst displays the best catalytic activity, with a T<sub>90</sub> of 177, 234, and 179 °C for CO, HC, and NO<sub>x</sub>, respectively. These values are lower than the T<sub>90</sub> values of 219, 276, and 220 °C for CO, HC, and NO<sub>x</sub> over the Pd/Al<sub>2</sub>O<sub>3</sub> catalyst, respectively. The metal–oxide interface is considered to play a prominent role in heterogeneous catalysis [43]. Analysis from the H<sub>2</sub>-TPR, XPS, and O<sub>2</sub>-TPD results indicates that the abundant Pd-CeO<sub>2</sub> interfacial sites could not only absorb more oxygen species but also possessed excellent low-temperature reducibility, contributing to the three-way reaction. In addition, to elucidate the impact and advantage of the Pd-CeO<sub>2</sub> interface produced by the L-arginine induction method on the activity of the Pd/Al<sub>2</sub>O<sub>3</sub>-xCeO<sub>2</sub> catalysts, the catalytic performance of the Pd/CeO<sub>2</sub> and Pd/Al<sub>2</sub>O<sub>3</sub>-2.4CeO<sub>2</sub>-JZ fresh catalysts was also investigated. The T<sub>90</sub> values of CO and HC oxidation and NO reduction over Pd/Al<sub>2</sub>O<sub>3</sub>-2.4CeO<sub>2</sub>-JZ were 237, 288, and 245 °C, respectively, showing that its performance was even worse than that of Pd/Al<sub>2</sub>O<sub>3</sub> in eliminating catalytic activity for the three pollutants. This may be due to poor selectivity, which failed to form an effective Pd-CeO<sub>2</sub> interfacial active site, leading to the blockage of the active site and reduced reaction activity. In addition, the T<sub>90</sub> values of CO and HC oxidation and NO<sub>x</sub> reduction over Pd/2.4CeO<sub>2</sub>-JZ were 198, 265, and 200 °C, respectively, which were also higher than the T<sub>90</sub> of the Pd/Al<sub>2</sub>O<sub>3</sub>-xCeO<sub>2</sub> catalysts. This indicates the formed Pd-CeO<sub>2</sub> interface activity site is much more than that of the Pd/CeO<sub>2</sub> catalyst prepared by traditional conventional synthesis methods, which have a limited-contact metal–oxide interface. In addition, the long-time stability test of the Pd/Al<sub>2</sub>O<sub>3</sub>-2.4CeO<sub>2</sub> catalyst was carried out. The Pd/Al<sub>2</sub>O<sub>3</sub>-2.4CeO<sub>2</sub> catalyst was evaluated by consecutively conducting the TWC test at 200 °C and 400 °C for 24 h, and it exhibited good thermal stability, as shown in Figure S11. The used Pd/Al<sub>2</sub>O<sub>3</sub>-2.4CeO<sub>2</sub> catalyst after the reaction was characterized by TEM as shown in Figure S12. The morphological structure and particle size of the nanoparticles barely changed, indicating the Pd/Al<sub>2</sub>O<sub>3</sub>-2.4CeO<sub>2</sub> catalyst possessed good catalytic stability.

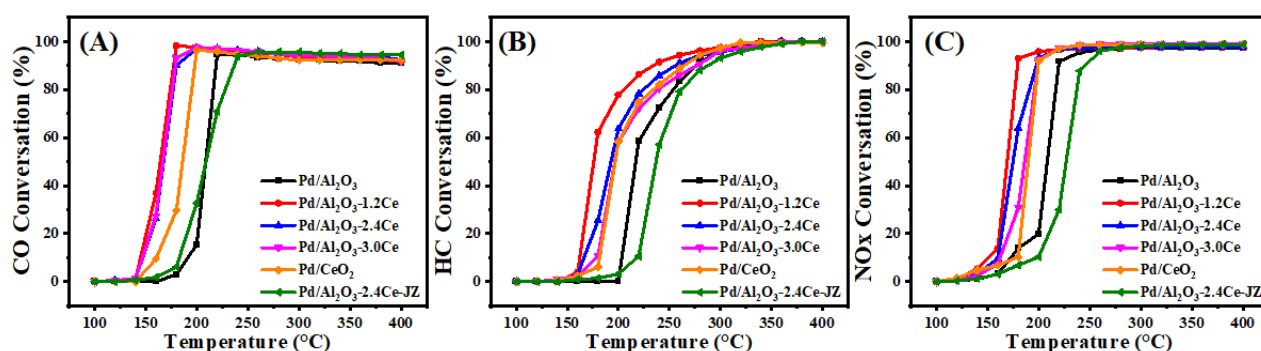


**Figure 4.** Conversions of CO (A), HC (B), and NO<sub>x</sub> (C) over fresh catalysts.

### 3.2. Characterization of Aged Catalysts

#### 3.2.1. Morphology Analysis

To further assess the thermal stability of the Pd/Al<sub>2</sub>O<sub>3</sub>-xCeO<sub>2</sub> catalysts, they were subjected to calcination at 900 °C in air for 5 h. The TEM and HRTEM images of the catalysts after calcination treatment are shown in Figure 5 and Figure S13. In the case of the aged Pd/Al<sub>2</sub>O<sub>3</sub> catalyst, there was a noticeable sintering of Pd NPs, with their size increasing from 4 nm to over 10 nm, which resulted in a significant loss of catalytic activity. For the aged Pd/Al<sub>2</sub>O<sub>3</sub>-xCeO<sub>2</sub> catalysts, the tiny CeO<sub>2</sub> particles showed a typical agglomeration phenomenon, with their size increasing beyond 15 nm. Concurrently, lattice fringes are observed in these catalysts, where the lattice spacings of 0.32 nm and 0.26 nm correspond to

the characteristic (111) or (200) planes of the fluorite phase  $\text{CeO}_2$ , respectively. In addition, it is hard to detect the Pd NPs by TEM and HRTEM, which are present in the catalysts, as confirmed by the result of the ICP-AES (Table S1).

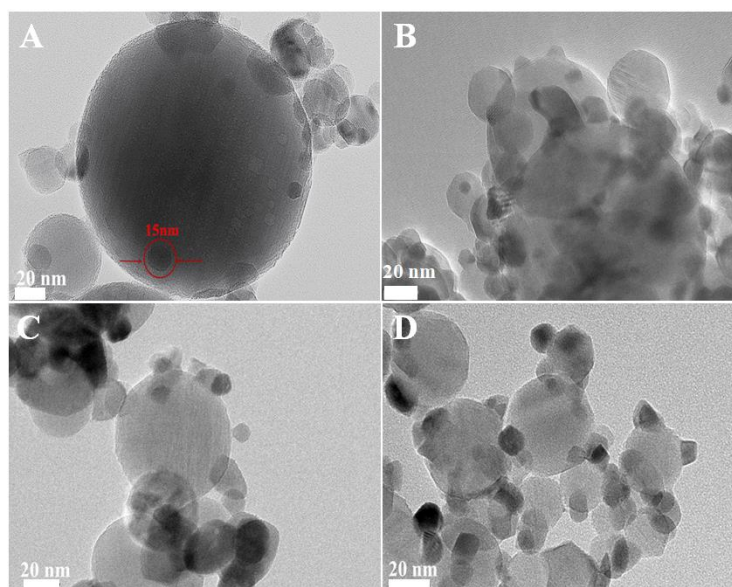


**Figure 5.** TEM of aged (A) Pd/ $\text{Al}_2\text{O}_3$ , (B) Pd/ $\text{Al}_2\text{O}_3$ -1.2 $\text{CeO}_2$ , (C) Pd/ $\text{Al}_2\text{O}_3$ -2.4 $\text{CeO}_2$ , (D) Pd/ $\text{Al}_2\text{O}_3$ -3.0 $\text{CeO}_2$  catalysts.

To clarify the distribution of Pd and  $\text{CeO}_2$  components after the aging treatment, EDS mapping analyses were carried out (Figure S14). However, only very few Pd species were detected, probably due to the highly dispersion of Pd species or Pd species being incorporated into the lattice of  $\text{CeO}_2$ . It is hypothesized that Pd species were fragmented into smaller particles that redispersed in the surface of  $\text{CeO}_2$  due to the strong interaction between Pd species and  $\text{CeO}_2$  [44].

### 3.2.2. Crystal Phase Analysis

Following the aging treatment at 900 °C, the crystallinity of the  $\text{Al}_2\text{O}_3$  remained largely unchanged, indicating that  $\text{Al}_2\text{O}_3$  is relatively stable under high-temperature conditions (Figure 6). In the case of the aged Pd/ $\text{Al}_2\text{O}_3$  catalyst, diffraction peaks for Pd were present at 34° (JCPDS No. 41-1107), albeit very weak, indicating that sintering had occurred in the Pd/ $\text{Al}_2\text{O}_3$  catalyst. For the aged Pd/ $\text{Al}_2\text{O}_3$ -x $\text{CeO}_2$  catalysts, no diffraction peaks of the Pd phase were observed, indicating that significant sintering of Pd did not take place, likely due to the dispersion of Pd species on the support or their incorporation into the  $\text{CeO}_2$  lattice. Combined with the results of the metal dispersion (Table 3), we can conclude that the Pd species were indeed highly dispersed on the support, leading to better thermal stability compared to the Pd/ $\text{Al}_2\text{O}_3$  catalysts. Regarding the  $\text{CeO}_2$  species, the full width at a half maximum of their characteristic peaks narrowed after the aging treatment, indicating that the  $\text{CeO}_2$  NPs grew larger and exhibited improved crystallization, which is consistent with the results calculated using the Scherrer equation.

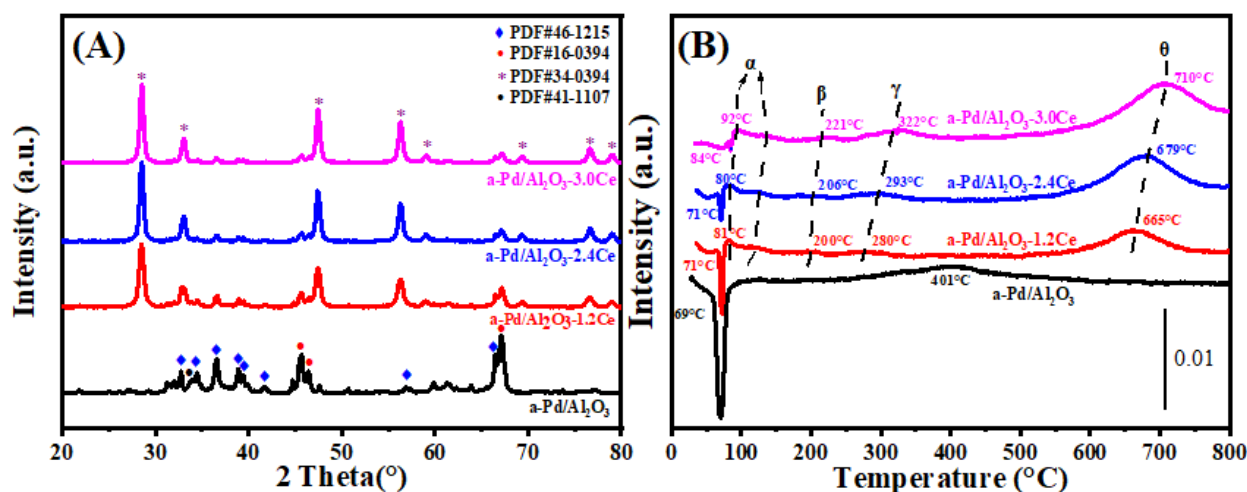


Figure 6. (A) XRD patterns and (B) H<sub>2</sub>-TPR profiles of the aged catalyst.

Table 3. BET surface areas, pore volumes, average sizes ( $D_{\text{CeO}_2}$ ), and dispersion of the aged catalysts.

Aged Catalysts	Surface Area ( $\text{m}^2 \cdot \text{g}^{-1}$ )	Pore Volume ( $\text{cm}^3 \cdot \text{g}^{-1}$ )	$D_{\text{CeO}_2}$ <sup>a</sup> (nm)	Dispersion of Pd <sup>b</sup> (%)
Pd/Al <sub>2</sub> O <sub>3</sub>	34	0.215	—	13.0
Pd/Al <sub>2</sub> O <sub>3</sub> -1.2CeO <sub>2</sub>	30	0.199	19.2	44.7
Pd/Al <sub>2</sub> O <sub>3</sub> -2.4CeO <sub>2</sub>	26	0.141	24.6	53.3
Pd/Al <sub>2</sub> O <sub>3</sub> -3.0CeO	31	0.136	25.8	58.4

<sup>a</sup> Data were obtained according to the Scherrer equation using the FWHM of CeO<sub>2</sub> in the XRD patterns. <sup>b</sup> Data were obtained by the CO pulse method.

### 3.2.3. Pore Structure Properties

Following the aging treatment at 900 °C, the surface area and total pore volume of Pd/Al<sub>2</sub>O<sub>3</sub>-xCeO<sub>2</sub> catalysts decreased and varied from 22 to 31 m<sup>2</sup>/g and from 0.124 to 0.199 cm<sup>3</sup>/g, respectively (Table 3), due to the sintering of CeO<sub>2</sub> particles. The surface area of the aged Pd/Al<sub>2</sub>O<sub>3</sub> catalyst showed no change, indicating the Al<sub>2</sub>O<sub>3</sub> support was stable in accordance with the results of XRD.

### 3.2.4. Low-Temperature Reducibility Analysis

The H<sub>2</sub>-TPR profiles for the aged Pd/Al<sub>2</sub>O<sub>3</sub> and Pd/Al<sub>2</sub>O<sub>3</sub>-xCeO<sub>2</sub> catalysts are displayed in Figure 6B. A negative peak in the range of 69–85 °C is observed for the aged catalysts, with the aged Pd/Al<sub>2</sub>O<sub>3</sub> sample exhibiting the most significant peak. This peak is generally attributed to the decomposition of palladium hydride, indicating the presence of larger Pd crystallites with an enhanced ability to adsorb H<sub>2</sub> via hydride formation [45]. Larger Pd particles exhibit more obvious decomposition peaks of palladium hydride, as hydride formation is a bulk phenomenon. The H<sub>2</sub> release for the negative peak follows the order: Pd/Al<sub>2</sub>O<sub>3</sub>-900 (80.9 μmol/g<sub>cat</sub>) > Pd/Al<sub>2</sub>O<sub>3</sub>-500 (26 μmol/g<sub>cat</sub>) > Pd/Al<sub>2</sub>O<sub>3</sub>-1.2CeO<sub>2</sub> (14.5 μmol/g<sub>cat</sub>) > Pd/Al<sub>2</sub>O<sub>3</sub>-2.4CeO<sub>2</sub> (4 μmol/g<sub>cat</sub>) > Pd/Al<sub>2</sub>O<sub>3</sub>-3.0CeO<sub>2</sub> (0.84 μmol/g<sub>cat</sub>). This indicates that the Pd species in Pd/Al<sub>2</sub>O<sub>3</sub>-xCeO<sub>2</sub> catalysts did not undergo severe sintering and maintained a higher dispersion, which is consistent with the results detected by the CO pulse method listed in Table 3. In comparison to the fresh Pd/Al<sub>2</sub>O<sub>3</sub> sample, an additional reduction peak emerges at 401 °C, with an H<sub>2</sub> consumption of 95.8 μmol/g<sub>cat</sub> for the aged Pd/Al<sub>2</sub>O<sub>3</sub> sample. This suggests that more PdO species were formed, which are difficult to reduce at low temperatures after calcination at 900 °C.

It is noteworthy that after the aging treatment, the intensity of the low-temperature reduction peaks ( $\alpha$ ) for the Pd/Al<sub>2</sub>O<sub>3</sub>-xCeO<sub>2</sub> catalysts was obviously reduced, and the

peaks shifted to higher temperatures. This is likely due to the severe sintering of CeO<sub>2</sub>, which may have disrupted the Pd-CeO<sub>2</sub> interface formed by the L-arginine induction method. However, aside from the Pd/Al<sub>2</sub>O<sub>3</sub>-1.2CeO<sub>2</sub> sample, the catalytic performance of the Pd/Al<sub>2</sub>O<sub>3</sub>-xCeO<sub>2</sub> catalysts did not change markedly after aging at 900 °C. The lower H<sub>2</sub> consumption of the negative peak and the higher dispersion of Pd species, as detected by the CO pulse method, suggest that no obvious sintering occurred for the Pd species. The reduction peaks ( $\beta$ ) correspond to the reduction of PdO<sub>x</sub> species that are embedded within the CeO<sub>2</sub> lattice in the form of a -Pd<sup>2+</sup>-O<sup>2-</sup>-Ce<sup>4+</sup> linkage, which occurs during the aging process [46]. The reduction peaks ( $\gamma$ ) shifted to lower temperatures, and the H<sub>2</sub> consumption decreased, possibly due to the high dispersion of Pd on CeO<sub>2</sub> and a reduction in the Pd-CeO<sub>2</sub> interface. In addition, the intensity of the reduction of peak ( $\theta$ ) increased, and peaks shifted to higher temperatures, which could be influenced by the dispersion state and sintering of CeO<sub>2</sub>. Additionally, the bulk reduction peaks of CeO<sub>2</sub> beyond 800 °C also shift to higher temperatures as a result of the severe sintering of CeO<sub>2</sub>.

Due to the interaction between Pd species and CeO<sub>2</sub>, leading to the Pd species being held in a high dispersion state, generally the higher Pd dispersion and smaller Pd particle size produce a higher active surface, resulting in a superior catalytic activity [29].

### 3.2.5. Surface Composition and Metal Chemical Analysis

Figure 7 illustrates the Al 2p, O 1s, Pd 3d, and Ce 3d XPS spectra of the fresh catalysts, with the surface element composition summarized in Table 4. The chemical states of Al 2p spectra remain almost unchanged before and after catalyst aging. Regarding the Ce 3d XPS spectra, both valence states of Ce<sup>3+</sup> and Ce<sup>4+</sup> continue to coexist in the catalyst, with no obvious decrease in the Ce<sup>3+</sup> concentration observed. This could be attributed to the incorporation of Pd NPs into the lattice of CeO<sub>2</sub> particles, leading to the generation of oxygen defects. Meanwhile, the O<sub>ads</sub>/O<sub>latt</sub> ratio increases compared to that of the fresh catalysts, indicating a decrease in lattice oxygen concentration and the creation of more oxygen defects [47]. Furthermore, after calcination at 900 °C in air, the Pd 3d value over the Pd/Al<sub>2</sub>O<sub>3</sub> catalyst shifts from 336.8 to 337.2 eV, indicating the formation of a higher oxidation state of Pd and the occurrence of the sintering phenomenon among Pd species during the aging process [48], which is in agreement with the result of the TEM images. For the Pd/Al<sub>2</sub>O<sub>3</sub>-xCeO<sub>2</sub> catalysts, there is a significant change in the peak position of Pd 3d, even if Pd enters the lattice of CeO<sub>2</sub> due to the similar binding energy of Ce<sub>1-x</sub>Pd<sub>x</sub>O<sub>2- $\delta$</sub>  solid solution around 337.9 eV [49–51]. At this point, the intensity of Pd/Al<sub>2</sub>O<sub>3</sub>-xCeO<sub>2</sub> catalysts increases, indicating the Pd species are highly dispersed on the surface of CeO<sub>2</sub>. This further confirms the strong interaction between Pd and CeO<sub>2</sub>.

**Table 4.** H<sub>2</sub> consumption and surface element composition of the aged catalysts.

Aged Catalysts	Reducibility of Fresh Catalysts (H <sub>2</sub> Consumption ( $\mu$ mol/gcat))				Aged-Surface Element Composition Molar Ratio (%)		
	Negative Peak	<200 °C	200–250 °C	250–350 °C	500–750 °C	O <sub>ads</sub> /O <sub>latt</sub>	Ce <sup>3+</sup> / (Ce <sup>3+</sup> + Ce <sup>4+</sup> )
a-Pd/Al <sub>2</sub> O <sub>3</sub>	−80.9	—	—	95.8	—	—	—
a-Pd/Al <sub>2</sub> O <sub>3</sub> -1.2CeO <sub>2</sub>	−14.5	11.9	2.6	9.0	112.9	21.8	15.9
a-Pd/Al <sub>2</sub> O <sub>3</sub> -2.4CeO <sub>2</sub>	−4.0	18.8	3.5	16.2	169.1	16.7	17.6
a-Pd/Al <sub>2</sub> O <sub>3</sub> -3.0CeO <sub>2</sub>	−0.84	24.9	3.9	29.7	185.4	7.2	18.1

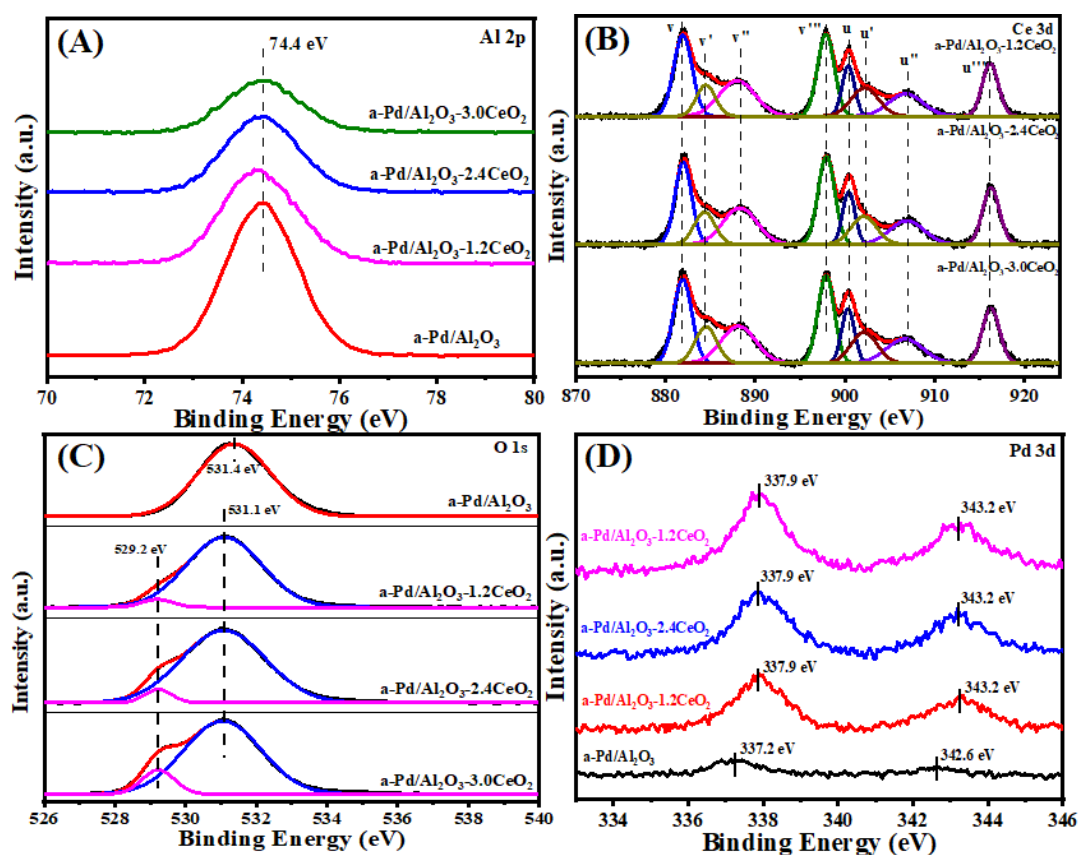


Figure 7. (A) Al 2p, (B) Ce 3d, (C) O 1s, and (D) Pd 3d XPS spectra of the aged catalysts.

### 3.2.6. Three-Way Catalytic Activities of Aged Catalysts

Figure 8 and Table S4 present the conversion results of CO, HC, and NO<sub>x</sub> under stoichiometric conditions over aged catalysts. After calcination at 900 °C, the  $T_{90}$  values for CO and HC oxidation and NO<sub>x</sub> reduction over the aged Pd/Al<sub>2</sub>O<sub>3</sub> catalysts increased by ~36, 104, and 139 °C, respectively, compared to the fresh samples. For the aged Pd/Al<sub>2</sub>O<sub>3</sub>-1.2CeO<sub>2</sub> catalysts, the  $T_{90}$  value for CO, HC, and NO increased by 41, 42, and 40 °C, respectively. The large change in the activity of the Pd/Al<sub>2</sub>O<sub>3</sub>-1.2CeO<sub>2</sub> catalyst may be due to the destruction of the Pd-CeO<sub>2</sub> interface and some sintering of the Pd nanoparticles. However, the catalytic activities of the aged Pd/Al<sub>2</sub>O<sub>3</sub>-2.4CeO<sub>2</sub> and Pd/Al<sub>2</sub>O<sub>3</sub>-3.0CeO<sub>2</sub> catalysts remained unchanged, except for an increase of about 20 °C in the  $T_{90}$  values for CO, indicating their outstanding thermal stability. Surprisingly, the  $T_{90}$  values for HC in the Pd/Al<sub>2</sub>O<sub>3</sub>-3.0CeO<sub>2</sub> catalyst decreased by about 35 °C. Combining the catalytic activity results with TEM images of the Pd/Al<sub>2</sub>O<sub>3</sub>-xCeO<sub>2</sub> catalysts, it was observed that Pd NPs could not be observed by HRTEM in those catalysts, which can be attributed to their high dispersion, consistent with the metal dispersion results. In addition, increasing the CeO<sub>2</sub> content enhances metal dispersion upon calcination at high temperatures. At the same time, some Pd species are incorporated into the CeO<sub>2</sub> lattice in the Pd/Al<sub>2</sub>O<sub>3</sub>-xCeO<sub>2</sub> catalysts, as evidenced by the Ce 3d and O 1s XPS spectra. In conclusion, the high dispersion of Pd species and the presence of a large number of oxygen vacancies are the key factors contributing to the better catalytic activities of the aged Pd/Al<sub>2</sub>O<sub>3</sub>-xCeO<sub>2</sub> catalysts after high-temperature treatment.

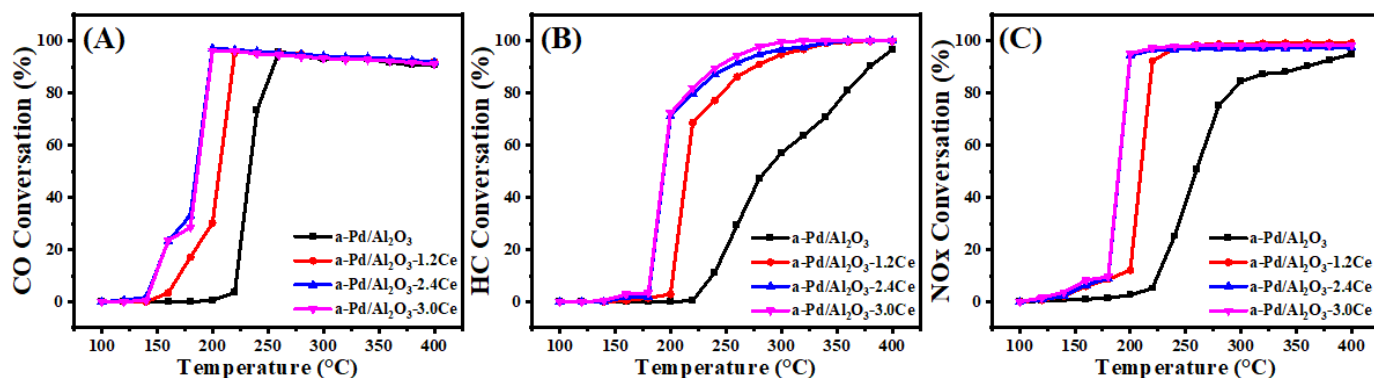


Figure 8. Conversion of CO (A), HC (B), and NO<sub>x</sub> (C) over the aged catalysts.

#### 4. Conclusions

We have successfully demonstrated a novel approach to precisely apply a catalyst, where CeO<sub>2</sub> selectively decorates Pd nanoparticles supported on Al<sub>2</sub>O<sub>3</sub> using the L-arginine induction method. This technique significantly enhances the catalytic activity and redox properties of the Pd/Al<sub>2</sub>O<sub>3</sub>-xCeO<sub>2</sub> catalyst by forming and expanding the contact interface between Pd and CeO<sub>2</sub>. EDS mapping confirmed that Pd nanoparticles were indeed selectively decorated by CeO<sub>2</sub>, creating the Pd-CeO<sub>2</sub> interface. O<sub>2</sub>-TPD and XPS results revealed that a larger amount of absorbed oxygen was present at the Pd-CeO<sub>2</sub> interface. After calcination at 900 °C for 5 h, the Pd/Al<sub>2</sub>O<sub>3</sub> catalyst underwent severe sintering, leading to a deterioration in redox properties. In contrast, the aged Pd/Al<sub>2</sub>O<sub>3</sub>-xCeO<sub>2</sub> catalyst showed, according to TEM, XRD, and BET results, that the CeO<sub>2</sub> severely sintered at high temperatures. However, Pd species were not detectable by XRD and TEM, indicating that there was no sintering phenomenon for the Pd species. XPS and metal dispersion studies revealed that Pd species were highly dispersed on the CeO<sub>2</sub> support, with some Pd species incorporated into the CeO<sub>2</sub> lattice, resulting in no significant change in the number of oxygen vacancies. Thus, it is evident that the metal–oxide interface and the metal–support interaction plays crucial roles in improving catalyst activity and promoting the redispersion of Pd species at high temperatures. This approach is an effective way to regulate catalytic activity and enhance the thermal stability of catalysts at elevated temperatures.

**Supplementary Materials:** The following supporting information can be downloaded at: <https://www.mdpi.com/article/10.3390/nano15030197/s1>, Figure S1: HRTEM image of irregular Pd nanoparticles; Figure S2: EDS mapping images of fresh 4 nm Pd/Al<sub>2</sub>O<sub>3</sub>-1.2CeO<sub>2</sub> catalyst; Figure S3: TEM images of 12 nm (A) and 19 nm (B) Pd nanoparticles; Figure S4: EDS mapping images of 12 nm Pd/Al<sub>2</sub>O<sub>3</sub>-1.2CeO<sub>2</sub> fresh catalyst; Figure S5: Local EDS mapping images of 12 nm Pd/Al<sub>2</sub>O<sub>3</sub>-1.2CeO<sub>2</sub> fresh catalyst; Figure S6: EDS mapping images of 19 nm Pd/Al<sub>2</sub>O<sub>3</sub>-1.2CeO<sub>2</sub> fresh catalyst; Figure S7: TEM images of Pd/Al<sub>2</sub>O<sub>3</sub>-2.4CeO<sub>2</sub>-JZ fresh catalyst; Figure S8: EDS mapping images of 19 nm Pd/Al<sub>2</sub>O<sub>3</sub>-2.4CeO<sub>2</sub>-JZ fresh catalyst; Figure S9: EDS mapping images of 19 nm Pd/Al<sub>2</sub>O<sub>3</sub>-1.2CeO<sub>2</sub>-JZ fresh catalyst; Figure S10: Adsorption–desorption isotherms of fresh catalysts; Figure S11: Long-time stability tests by Pd/Al<sub>2</sub>O<sub>3</sub>-2.4CeO<sub>2</sub> catalyst at 200 °C (A) and 400 °C (B); Figure S12: TEM images of used Pd/Al<sub>2</sub>O<sub>3</sub>-2.4CeO<sub>2</sub> catalyst after long-time stability tests at 400 °C for 24 h; Figure S13: HRTEM images of aged (A) Pd/Al<sub>2</sub>O<sub>3</sub>-1.2CeO<sub>2</sub>, (B) Pd/Al<sub>2</sub>O<sub>3</sub>-2.4CeO<sub>2</sub>, and (C) Pd/Al<sub>2</sub>O<sub>3</sub>-3.0CeO<sub>2</sub> catalysts; Figure S14: EDS mapping images of aged Pd/Al<sub>2</sub>O<sub>3</sub>-1.2CeO<sub>2</sub> catalysts; Table S1: Real loading of Pd determined by the ICP-AES technique; Table S2: Oxygen desorption of the fresh catalysts; Table S3: The temperature required to reach 90% conversion of CO, HC, and NO over fresh catalysts; Table S4: The temperature required to reach 90% conversion of CO, HC, and NO over aged catalysts.

**Author Contributions:** Conceptualization, Z.L. (Ziwen Liu); Methodology, Z.L. (Ziwen Liu); Formal analysis, Z.L. (Ziwen Liu) and L.N.; Investigation, Z.L. (Ziwen Liu) and L.N.; Resources, Z.L.

(Zhenguo Li) and H.H.; Data curation, Z.L. (Ziwen Liu) and L.N.; Writing—original draft, Z.L. (Ziwen Liu); Writing—review & editing, Z.S., Z.L. (Zhenguo Li) and H.H.; Supervision, G.Z.; Project administration, G.Z.; Funding acquisition, G.Z. and H.H. All authors have read and agreed to the published version of the manuscript.

**Funding:** This work was supported by the National Engineering Laboratory for Mobile Source Emission Control Technology NELMS2019A04 and NSFC 22035009.

**Data Availability Statement:** Data are contained within this article.

**Conflicts of Interest:** Author Ziwen Liu was employed by the company Sinopec Catalyst Co., Ltd., the author Lijuan Niu was employed by the company Carbon Energy Technology Co., Ltd., and the author Zhenguo Li was employed by the company China Automotive Technology and Research Center Co., Ltd. The remaining authors declare that the research was conducted in the absence of any commercial or financial relationships that could be construed as a potential conflict of interest.

## References

1. Jin, M.; Liu, H.; Zhang, H.; Xie, Z.; Liu, J.; Xia, Y. Synthesis of Pd nanocrystals enclosed by {100} facets and with sizes <10 nm for application in CO oxidation. *Nano Res.* **2011**, *4*, 83–91.
2. Tang, H.; Wei, J.; Liu, F.; Qiao, B.; Pan, X.; Li, L.; Liu, J.; Wang, J.; Zhang, T. Strong metal–support interactions between gold nanoparticles and nonoxides. *J. Am. Chem. Soc.* **2016**, *138*, 56–59. [[CrossRef](#)]
3. An, K.; Alayoglu, S.; Musselwhite, N.; Plamthottam, S.; Melaet, G.; Lindeman, A.E.; Somorjai, G.A. Enhanced Co oxidation rates at the interface of mesoporous oxides and Pt nanoparticles. *J. Am. Chem. Soc.* **2013**, *135*, 16689–16696. [[CrossRef](#)] [[PubMed](#)]
4. Zhang, Z.; Xu, B.; Wang, X. Engineering nanointerfaces for nanocatalysis. *Chem. Soc. Rev.* **2014**, *43*, 7870–7886. [[CrossRef](#)]
5. Kang, S.B.; Lim, J.B.; Jo, D.; Nam, I.; Cho, B.K.; Hong, S.B.; Kim, C.H.; Oh, S.H. Ostwald-ripening sintering kinetics of Pd-based three-way catalyst: Importance of initial particle size of Pd. *Chem. Eng. J.* **2017**, *316*, 631–644. [[CrossRef](#)]
6. Hansen, T.W.; Delariva, A.T.; Challa, S.R.; Datye, A.K. Sintering of catalytic nanoparticles: Particle migration or Ostwald ripening? *Acc. Chem. Res.* **2013**, *46*, 1720–1730. [[CrossRef](#)] [[PubMed](#)]
7. Zhang, Z.; Fan, Y.; Xin, Y.; Li, Q.; Li, R.; Anderson, J.A.; Zhang, Z. Improvement of air/fuel ratio operating window and hydrothermal stability for Pd-only three-way catalysts through a Pd–Ce<sub>2</sub>Zr<sub>2</sub>O<sub>8</sub> superstructure interaction. *Environ. Sci. Technol.* **2015**, *49*, 7989–7995. [[CrossRef](#)]
8. Lan, L.; Li, H.; Chen, S.; Chen, Y. Preparation of CeO<sub>2</sub>–ZrO<sub>2</sub>–Al<sub>2</sub>O<sub>3</sub> composite with layered structure for improved Pd-only three-way catalyst. *J. Mater. Sci.* **2017**, *52*, 9615–9629. [[CrossRef](#)]
9. Montini, T.; Melchionna, M.; Monai, M.; Fornasiero, P. Fundamentals and catalytic applications of CeO<sub>2</sub>-based materials. *Chem. Rev.* **2016**, *116*, 5987–6041. [[CrossRef](#)]
10. Li, L.; Zhang, N.; Huang, X.; Liu, Y.; Li, Y.; Zhang, G.; Song, L.; He, H. Hydrothermal stability of core–shell Pd@Ce<sub>0.5</sub>Zr<sub>0.5</sub>O<sub>2</sub>/Al<sub>2</sub>O<sub>3</sub> catalyst for automobile three-way reaction. *ACS Catal.* **2018**, *8*, 3222–3231. [[CrossRef](#)]
11. Shinjoh, H. Noble metal sintering suppression technology in three-way catalyst: Automotive three-way catalysts with the noble metal sintering suppression technology based on the support anchoring effect. *Catal. Surv. Asia* **2009**, *13*, 184–190. [[CrossRef](#)]
12. Joo, S.H.; Park, J.Y.; Tsung, C.; Yamada, Y.; Yang, P.; Somorjai, G.A. Thermally stable Pt/mesoporous silica core–shell nanocatalysts for high-temperature reactions. *Nat. Mater.* **2009**, *8*, 126–131. [[CrossRef](#)]
13. Arnal, P.M.; Comotti, M.; Schüth, F. High-temperature-stable catalysts by hollow sphere encapsulation. *Angew. Chem. Int. Ed.* **2006**, *45*, 8224–8227. [[CrossRef](#)] [[PubMed](#)]
14. Sun, M.; Fu, Q.; Gao, L.; Zheng, Y.; Li, Y.; Chen, M.; Bao, X. Catalysis under shell: Improved CO oxidation reaction confined in Pt@h-BN core–shell nanoreactors. *Nano Res.* **2017**, *10*, 1403–1412. [[CrossRef](#)]
15. Sun, Z.; Zhang, H.; Zhao, Y.; Huang, C.; Tao, R.; Liu, Z.; Wu, Z. Thermal-stable carbon nanotube-supported metal nanocatalysts by mesoporous silica coating. *Langmuir* **2011**, *27*, 6244–6251. [[CrossRef](#)] [[PubMed](#)]
16. Hu, Y.; Tao, K.; Wu, C.; Zhou, C.; Yin, H.; Zhou, S. Size-controlled synthesis of highly stable and active Pd@SiO<sub>2</sub> core–shell nanocatalysts for hydrogenation of nitrobenzene. *J. Phys. Chem. C* **2013**, *117*, 8974–8982. [[CrossRef](#)]
17. Zhang, J.; Li, F. Coke-resistant Ni@SiO<sub>2</sub> catalyst for dry reforming of methane. *Appl. Catal. B Environ.* **2015**, *176–177*, 513–521. [[CrossRef](#)]
18. Yang, J.; Zhang, F.; Chen, Y.; Qian, S.; Hu, P.; Li, W.; Deng, Y.; Fang, Y.; Han, L.; Luqman, M.; et al. Core-shell Ag@SiO<sub>2</sub>@m SiO<sub>2</sub> mesoporous nanocarriers for metal-enhanced fluorescence. *Chem. Commun.* **2011**, *47*, 11618–11620. [[CrossRef](#)] [[PubMed](#)]
19. Li, L.; He, S.; Song, Y.; Zhao, J.; Ji, W.; Au, C. Fine-tunable Ni@porous silica core–shell nanocatalysts: Synthesis, characterization, and catalytic properties in partial oxidation of methane to syngas. *J. Catal.* **2012**, *288*, 54–64. [[CrossRef](#)]



20. Forman, A.J.; Park, J.; Tang, W.; Hu, Y.; Stucky, G.D.; McFarland, E.W. Silica-encapsulated Pd nanoparticles as a regenerable and sintering-resistant catalyst. *ChemCatChem* **2010**, *2*, 1318–1324. [[CrossRef](#)]
21. Lu, J.; Fu, B.; Kung, M.C.; Xiao, G.; Elam, J.W.; Kung, H.H.; Stair, P.C. Coking- and sintering-resistant palladium catalysts achieved through atomic layer deposition. *Science* **2012**, *335*, 1205–1208. [[CrossRef](#)] [[PubMed](#)]
22. Liu, Z.; Niu, L.; Zong, X.; An, L.; Qu, D.; Wang, X.; Sun, Z. Ambient photothermal catalytic CO oxidation over a carbon-supported palladium catalyst. *Appl. Catal. B Environ.* **2022**, *313*, 121439. [[CrossRef](#)]
23. Babu, N.S.; Lingaiah, N.; Gopinath, R.; Sankar Reddy, P.S.; Sai Prasad, P.S. Characterization and reactivity of alumina-supported Pd catalysts for the room-temperature hydrodechlorination of chlorobenzene. *J. Phys. Chem. C* **2007**, *111*, 6447–6453. [[CrossRef](#)]
24. Barrera, A.; Viniegra, M.; Fuentes, S.; Díaz, G. The role of lanthana loading on the catalytic properties of Pd/Al<sub>2</sub>O<sub>3</sub>-La<sub>2</sub>O<sub>3</sub> in the NO reduction with H<sub>2</sub>. *Appl. Catal. B Environ.* **2005**, *56*, 279–288. [[CrossRef](#)]
25. Shen, M.; Yang, M.; Wang, J.; Wen, J.; Zhao, M.; Wang, W. Pd/support interface-promoted Pd–Ce<sub>0.7</sub>Zr<sub>0.3</sub>O<sub>2</sub>–Al<sub>2</sub>O<sub>3</sub> automobile three-way catalysts: Studying the dynamic oxygen storage capacity and CO, C<sub>3</sub>H<sub>8</sub>, and NO conversion. *J. Phys. Chem. C* **2009**, *113*, 3212–3221. [[CrossRef](#)]
26. Xie, S.; Liu, Y.; Deng, J.; Zhao, X.; Yang, J.; Zhang, K.; Han, Z.; Dai, H. Three-dimensionally ordered macroporous CeO<sub>2</sub>-supported Pd@Co nanoparticles: Highly active catalysts for methane oxidation. *J. Catal.* **2016**, *342*, 17–26. [[CrossRef](#)]
27. Chen, Q.; Li, N.; Luo, M.; Lu, J. Catalytic oxidation of dichloromethane over Pt/CeO<sub>2</sub>-Al<sub>2</sub>O<sub>3</sub> catalysts. *Appl. Catal. B Environ.* **2012**, *127*, 159–166. [[CrossRef](#)]
28. Meng, M.; Lin, P.; Fu, Y. The catalytic removal of CO and NO over Co-Pt(Pd, Rh)/γ-Al<sub>2</sub>O<sub>3</sub> catalysts and their structural characterizations. *Catal. Lett.* **1997**, *48*, 213–222. [[CrossRef](#)]
29. Luo, Y.; Xiao, Y.; Cai, G.; Zheng, Y.; Wei, K. Complete methanol oxidation in carbon monoxide streams over Pd/CeO<sub>2</sub> catalysts: Correlation between activity and properties. *Appl. Catal. B Environ.* **2013**, *136–137*, 317–324. [[CrossRef](#)]
30. He, H.; Gao, C. A general strategy for the preparation of carbon nanotubes and graphene oxide decorated with PdO nanoparticles in water. *Molecules* **2010**, *15*, 4679–4694. [[CrossRef](#)]
31. Zhou, R.; Zhao, B.; Yue, B. Effects of CeO<sub>2</sub>-ZrO<sub>2</sub> present in Pd/Al<sub>2</sub>O<sub>3</sub> catalysts on the redox behavior of PdOx and their combustion activity. *Appl. Surf. Sci.* **2008**, *254*, 4701–4707. [[CrossRef](#)]
32. Gil, S.; Garcia-Vargas, J.; Liotta, L.; Pantaleo, G.; Ousmane, M.; Retailleau, L.; Giroir-Fendler, A. Catalytic oxidation of propene over Pd catalysts supported on CeO<sub>2</sub>, TiO<sub>2</sub>, Al<sub>2</sub>O<sub>3</sub> and M/Al<sub>2</sub>O<sub>3</sub> oxides (m = Ce, Ti, Fe, Mn). *Catalysts* **2015**, *5*, 671–689. [[CrossRef](#)]
33. Mazzieri, V.; Coloma-Pascual, F.; Arcoya, A.; Argentièrre, P.C.L.; Fi, X.; Goli, N.S. XPS, FTIR and TPR characterization of Ru/Al<sub>2</sub>O<sub>3</sub> catalysts. *Appl. Surf. Sci.* **2003**, *210*, 222–230. [[CrossRef](#)]
34. Wei, Y.; Liu, J.; Zhao, Z.; Duan, A.; Jiang, G. The catalysts of three-dimensionally ordered macroporous Ce<sub>1-x</sub>Zr<sub>x</sub>O<sub>2</sub>-supported gold nanoparticles for soot combustion: The metal–support interaction. *J. Catal.* **2012**, *287*, 13–29. [[CrossRef](#)]
35. Zhao, B.; Li, G.; Ge, C.; Wang, Q.; Zhou, R. Preparation of Ce<sub>0.67</sub>Zr<sub>0.33</sub>O<sub>2</sub> mixed oxides as supports of improved Pd-only three-way catalysts. *Appl. Catal. B Environ.* **2010**, *96*, 338–349. [[CrossRef](#)]
36. Lan, L.; Chen, S.; Zhao, M.; Gong, M.; Chen, Y. The effect of synthesis method on the properties and catalytic performance of Pd/Ce<sub>0.5</sub>Zr<sub>0.5</sub>O<sub>2</sub>-Al<sub>2</sub>O<sub>3</sub> three-way catalyst. *J. Mol. Catal. A Chem.* **2014**, *394*, 10–21. [[CrossRef](#)]
37. Fan, J.; Wu, X.; Wu, X.; Liang, Q.; Ran, R.; Weng, D. Thermal ageing of Pt on low-surface-area CeO<sub>2</sub>-ZrO<sub>2</sub>-La<sub>2</sub>O<sub>3</sub> mixed oxides: Effect on the OSC performance. *Appl. Catal. B Environ.* **2008**, *81*, 38–48. [[CrossRef](#)]
38. Wang, B.; Weng, D.; Wu, X.; Ran, R. Modification of Pd–CeO<sub>2</sub> catalyst by different treatments: Effect on the structure and CO oxidation activity. *Appl. Surf. Sci.* **2011**, *257*, 3878–3883. [[CrossRef](#)]
39. Tan, H.; Wang, J.; Yu, S.; Zhou, K. Support morphology-dependent catalytic activity of Pd/CeO<sub>2</sub> for formaldehyde oxidation. *Environ. Sci. Technol.* **2015**, *49*, 8675–8682. [[CrossRef](#)]
40. Ivanova, A.S.; Slavinskaya, E.M.; Gulyaev, R.V.; Zaikovskii, V.I.; Stonkus, O.A.; Danilova, I.G.; Plyasova, L.M.; Polukhina, I.A.; Boronin, A.I. Metal–support interactions in Pt/Al<sub>2</sub>O<sub>3</sub> and Pd/Al<sub>2</sub>O<sub>3</sub> catalysts for CO oxidation. *Appl. Catal. B Environ.* **2010**, *97*, 57–71. [[CrossRef](#)]
41. Lin, S.; Yang, L.; Yang, X.; Zhou, R. Redox properties and metal–support interaction of Pd/Ce<sub>0.67</sub>Zr<sub>0.33</sub>O<sub>2</sub>-Al<sub>2</sub>O<sub>3</sub> catalyst for CO, HC and NOx elimination. *Appl. Surf. Sci.* **2014**, *305*, 642–649. [[CrossRef](#)]
42. Hegde, M.S.; Bera, P. Noble metal ion substituted CeO<sub>2</sub> catalysts: Electronic interaction between noble metal ions and CeO<sub>2</sub> lattice. *Catal. Today* **2015**, *253*, 40–50. [[CrossRef](#)]
43. Wang, M.; Gao, Z.; Zhang, B.; Yang, H.; Qiao, Y.; Chen, S.; Ge, H.; Zhang, J.; Qin, Y. Ultrathin coating of confined Pt nanocatalysts by atomic layer deposition for enhanced catalytic performance in hydrogenation reactions. *Chem.—Eur. J.* **2016**, *22*, 8438–8443. [[CrossRef](#)] [[PubMed](#)]
44. Hinokuma, S.; Fujii, H.; Okamoto, M.; Ikeue, K.; Machida, M. Metallic Pd nanoparticles formed by Pd–O–Ce interaction: A reason for sintering-induced activation for CO oxidation. *Chem. Mater.* **2010**, *22*, 6183–6190. [[CrossRef](#)]
45. Zheng, Q.; Farrauto, R.; Deeba, M. Part ii: Oxidative thermal aging of Pd/Al<sub>2</sub>O<sub>3</sub> and Pd/Ce<sub>x</sub>O<sub>y</sub>-ZrO<sub>2</sub> in automotive three way catalysts: The effects of fuel shutoff and attempted fuel rich regeneration. *Catalysts* **2015**, *5*, 1797–1814. [[CrossRef](#)]

46. Meng, L.; Jia, A.; Lu, J.; Luo, L.; Huang, W.; Luo, M. Synergetic effects of PdO species on CO oxidation over PdO–CeO<sub>2</sub> catalysts. *J. Phys. Chem. C* **2011**, *115*, 19789–19796. [[CrossRef](#)]
47. Aliotta, C.; Liotta, L.F.; La Parola, V.; Martorana, A.; Muccillo, E.N.S.; Muccillo, R.; Deganello, F. Ceria-based electrolytes prepared by solution combustion synthesis: The role of fuel on the materials properties. *Appl. Catal. B Environ.* **2016**, *197*, 14–22. [[CrossRef](#)]
48. Wu, X.; Xu, L.; Weng, D. The thermal stability and catalytic performance of Ce-Zr promoted Rh-Pd/ $\gamma$ -Al<sub>2</sub>O<sub>3</sub> automotive catalysts. *Appl. Surf. Sci.* **2004**, *221*, 375–383. [[CrossRef](#)]
49. Priolkar, K.R.; Bera, P.; Sarode, P.R.; Hegde, M.S.; Emura, S.; Kumashiro, R.; Lalla, N.P. Formation of Ce<sub>1-x</sub>Pd<sub>x</sub>O<sub>2- $\delta$</sub>  solid solution in combustion-synthesized Pd/CeO<sub>2</sub> catalyst: XRD, XPS, and EXAFS investigation. *Chem. Mater.* **2002**, *14*, 2120–2128. [[CrossRef](#)]
50. Li, G.; Li, L.; Yuan, Y.; Shi, J.; Yuan, Y.; Li, Y.; Zhao, W.; Shi, J. Highly efficient mesoporous Pd/CeO<sub>2</sub> catalyst for low temperature co oxidation especially under moisture condition. *Appl. Catal. B Environ.* **2014**, *158–159*, 341–347. [[CrossRef](#)]
51. Adijanto, L.; Sampath, A.; Yu, A.S.; Cargnello, M.; Fornasiero, P.; Gorte, R.J.; Vohs, J.M. Synthesis and stability of Pd@CeO<sub>2</sub> core–shell catalyst films in solid oxide fuel cell anodes. *ACS Catal.* **2013**, *3*, 1801–1809. [[CrossRef](#)]

**Disclaimer/Publisher’s Note:** The statements, opinions and data contained in all publications are solely those of the individual author(s) and contributor(s) and not of MDPI and/or the editor(s). MDPI and/or the editor(s) disclaim responsibility for any injury to people or property resulting from any ideas, methods, instructions or products referred to in the content.